

An Integrated Approach to Study Cement-to-Formation Bonding

Arpita P. Bathija *  and Peter J. Boul

Houston Research Center, Aramco Americas, 16300 Park Row Blvd, Houston, TX 77084, USA

* Correspondence: arpita.bathija@aramcoamericas.com

Abstract: It is crucial to assess the bond strength of the cement–formation interface while developing novel cements for efficient zonal isolation. An integrated method is presented to investigate the failure mechanism in cement and formation rock under downhole reservoir temperature and pressure conditions using a triaxial experimental setup. The acoustic emission count, strain, and velocity data aid in inferring the fracture process that led to the failure of a specimen. Although most specimens investigated exhibit the three dominant events of compaction, multi-cracking, and sliding, there are variations in the basic structure of each specimen. Furthermore, the insight obtained about the internal structure of the specimen points to its strength and damage tolerance, both of which are vital requirements for bonding. This method can distinguish between a standard cement and modified cement very effectively and help in pairing the appropriate cement formulation for a formation rock.

Keywords: cement bond strength; cement shear bond; oil-well cementing



Citation: Bathija, A.P.; Boul, P.J. An Integrated Approach to Study Cement-to-Formation Bonding. *Energies* **2022**, *15*, 5949. <https://doi.org/10.3390/en15165949>

Academic Editor: Shu Tao

Received: 7 July 2022

Accepted: 14 August 2022

Published: 17 August 2022

Publisher's Note: MDPI stays neutral with regard to jurisdictional claims in published maps and institutional affiliations.



Copyright: © 2022 by the authors. Licensee MDPI, Basel, Switzerland. This article is an open access article distributed under the terms and conditions of the Creative Commons Attribution (CC BY) license (<https://creativecommons.org/licenses/by/4.0/>).

1. Introduction

From the well construction phase to the well abandonment phase, poor cementation makes it difficult to achieve effective zonal isolation due to debonding at the interfaces of cements and rock formations. Stress fluctuations, thermal shocks, stimulation treatments, casing shrinkage/expansion during shut down or restart of production, chemical attack, wettability variations, and surface conditions of the casing and formation are all factors for cement bond failure [1–5].

The ability to isolate different geologic zones with varying pore pressures and fluid/gas chemistries, as well as the ability to prevent uncontrolled migration of pore fluids to shallower depths, is called zonal isolation. Cement shear bond strength measurements are used to evaluate a particularly important aspect of the cement's ability to provide effective zonal isolation [6]. Cement's bonding strength to casing and formations was studied extensively [2,7–10].

Testing the compressive strength of cubic cement samples on a loading frame where the vertical load is increased at a constant rate until the sample fails is a recommended practice [11]. Ultrasonic cement analyzers (UCA) employ a sonic nondestructive testing technique to correlate compressive strength to sonic compressional transit time. Strength correlations are specific to certain cement compositions. Although this common UCA approach is quick, simple, and API-recommended, new cement compositions may not fit the manufacturer's correlations, necessitating bespoke correlations.

Several push-out experiments were performed to determine shear bond strength, in which the cement is set with a cylindrical rock or casing sample within [12]. A load frame is used to apply a vertical load on the rock until it separates from the cement. Another approach is to create a composite core by vertically setting cement on top of a cylindrical rock [4]. The composite core is then loaded in the direction parallel to the bonding surface until failure. Earlier experimental methods for evaluating new cements were difficult to apply in a consistent and repeatable manner for all rock types. Separating the shear force to determine the shear bond strength is challenging and inconclusive because multiple forces act at the contact [13,14].

Our work will build upon that of researchers [14] wherein cement and shale samples were prepared with a 60° contacting angle for basic compressive strength testing in an unconfined and ambient laboratory condition. We are measuring the cement-to-formation shear bond strength while also monitoring velocities, acoustic emissions, and strain at downhole reservoir conditions. We have a quantitative analysis of the shear bond failure between the cement and the rock, as well as a value for the shear bond strength. Quantitative analysis gives us an insight into the strength and damage tolerance of the specimen.

2. Methodology

Two very different formations, the Berea and Torrey sandstones were used to demonstrate the method's applicability. Table 1 shows the mean values for porosity measured using Boyle's law helium porosimeter, permeability measured with flowing nitrogen, and grain densities. Berea [15] has higher permeability and porosity than Torrey, as shown in Table 1.

Table 1. Mean porosity, permeability, and grain density of formations.

Formation	Porosity (%)	Permeability (mD)		Grain Density (g/cc)
		k _{air}	Klinkenberg	
Berea	24.6	826	785	2.65
Torrey	17.7	3.33	2.74	2.73

Table 2 shows the results of the X-ray diffraction analysis. A PANalytical X'PertPro X-ray diffractometer was used to examine the mineral content of both the formations. Quartz is the main component in both sandstones. Torrey has 30% dolomite, whereas Berea [15] contains trace amounts of carbonate minerals.

Table 2. X-ray diffraction analysis results. Tr ≤ 0.5%.

Formation	Clay Minerals (wt.%)			Other Minerals (wt.%)			Carbonate Minerals (wt.%)			Totals (wt.%)		
	Illite-Smectite	Illite/Mica	Kaolinite	Quartz	K-Feldspar	Plagioclase	Pyrite	Calcite	Dolomite	Clay	Other	Carbonate
Berea	Tr	1	3	95	1	Tr	Tr	Tr	Tr	4	96	Tr
Torrey	Tr	3	9	54	5	Tr	Tr	Tr	29	12	59	29

API Class G cement [16,17] was used in the study as pure cement. Coring cylindrical formation specimens (2 inches in diameter by 4.5 inches in height) is the first step in the sample preparation process. A composite specimen is prepared by cutting the aforementioned formation specimen in half at a 60° angle from the horizontal direction [15]. Laboratory data, field results, and acoustic logs emphasize the change in cement bonding with roughness [8]. Hence, a preset cutting speed was used to control the roughness of the formation interface to achieve consistent results. Before setting the cement, the surface roughness was measured using an optical profiler (Nanovea). Berea was found to have a roughness of 230 ± 47 micrometers. It was verified that using the same cutting tool at a preset speed consistently maintained the surface roughness.

The method of preparing cement and formation samples with a 60° contacting angle is based on the theory of rock strength [18,19]. The theory estimates the angle of the bedding planes that lower the rock strength [20] (pp. 105–107). According to this theory, a slip on a bedding plane at a 60° angle would occur at a far lower stress level than that required to

generate a new fault. It was verified experimentally [21] that foliation planes at this angle have the maximum effect, reducing the rock strength by 50%.

Cement was prepared according to the standard recommended procedure [11]. The prepared cement was poured into a cylindrical mold on top of the cut core specimen. The molds were cured for three days at 180 °F and 20.68 MPa. Another specimen (improved cement) was prepared by mixing API Class G cement with silica flour (35% by weight of cement). Improved cement (silica flour is known to improve cement by reducing shrinkage) was cured at 300 °F and 20.68 MPa. The cured specimen was trimmed to achieve a length-to-diameter ratio of at least two. Special attention was paid to maintaining equal amounts of cement and formation in the composite specimen. Figure 1a shows one of our composite specimens cured with API Class G cement and Berea cut at 60° to the horizontal plane, which is the weakest plane of failure. The ends of the specimen were paralleled for precise velocity acquisition. The specimen was wrapped in a copper sleeve for protection from confining fluid at 6.89 MPa. Vertical and horizontal strain gauges were attached to the specimen. Input wires were soldered to the strain gauges for monitoring deformation. Endcaps with acoustic transducers were attached on both ends of the specimen. The specimen was then placed in the triaxial experimental setup (Autolab 3000, NER), as shown in Figure 2, and all the wires properly connected to the feed-thrus for data acquisition. A constant confining pressure (P_c) of 10 megapascals (MPa) was applied at room temperature and reading calibrations were performed [22]. The cement curing (temperature and pressure) and data acquisition conditions (axial stress, confining pressure, and temperature) may be adjusted to match the reservoir conditions of interest. At a P_c of 10 MPa, a vertical compressive force was applied at a constant rate of 0.01 MPa per second until the specimen failed. Velocities, specimen deformation, and acoustic emission counts were measured at regular intervals. It should be noted that the measurements and data analyses were performed on multiple samples of each kind and the standard deviation in the data are also presented.

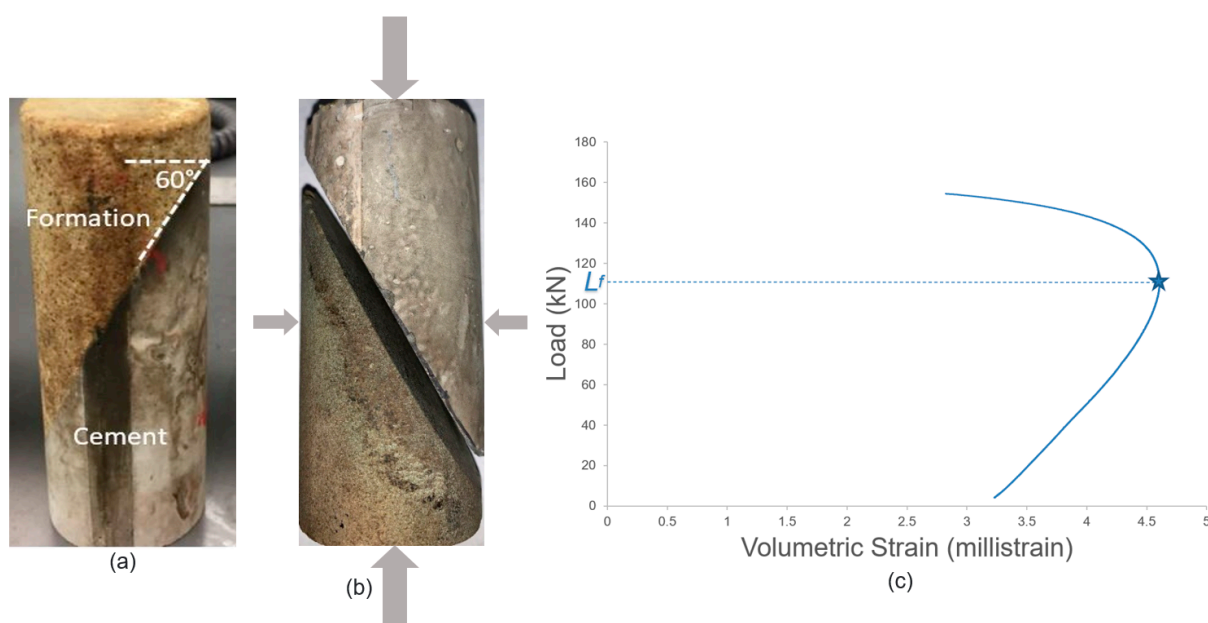


Figure 1. Failure in composite specimen. (a) Prior to setting the cement, the formation was cut at 60° to the horizontal in a composite specimen. (b) The composite specimen of cement (top) and Berea (bottom). Arrows indicate the direction of applied stresses. Vertical axial stress is applied, as well as confining stress all around the specimen. The size of the arrows indicates the relative magnitudes of the stresses that caused the shear failure. (c) Load versus volumetric strain data obtained from one of our specimens. Failure in a specimen is recognized when volumetric strain rolls over (at the star point).

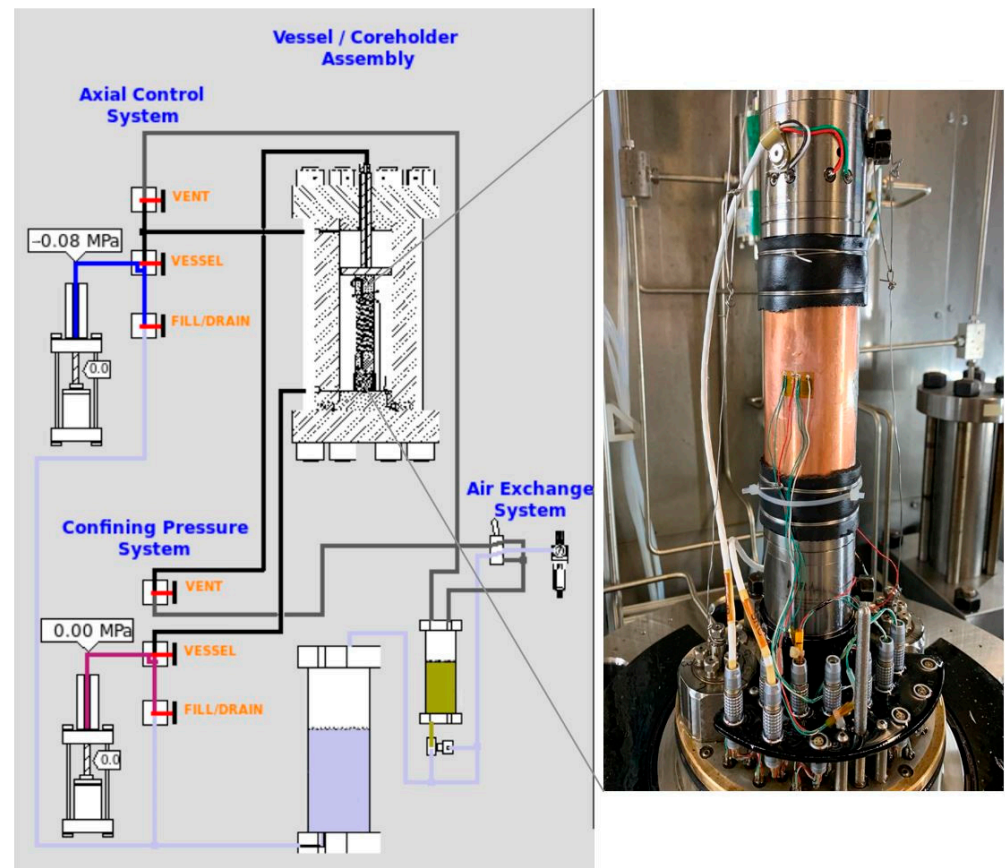


Figure 2. Triaxial experimental setup to pressurize the sample with confining and axial stress. An inset with a fully connected sample is shown.

The compressive strength (CS) at confined conditions (P_c) is the differential stress (axial stress P_c) at which the specimen fails. Figure 1b depicts one of our failed samples owing to interfacial shear slip. Figure 1c demonstrates that failure in a specimen is recognized when volumetric strain rolls over, giving us the load at failure (L_f). The shear bond strength may be obtained by dividing the shear force applied to the interface at failure by the interfacial area [14]. Figure 3 is reproduced with permission of the Cambridge University Press through PLSclear. We know the exact failure plane area with $\beta = 60^\circ$ in the composite specimen (Figure 3a), where β is the angle between the maximum compressive stress (σ_1) and the normal to the fault. It is difficult to determine the failure plane for the whole cement or formation specimen, resulting in inaccurate shear strength measurements. Figure 3b [20] (p. 88) shows that the shear force can be calculated based on the Mohr–Coulomb failure analysis as:

$$\tau_f = \frac{L_f \sin 60^\circ \cos 60^\circ}{\pi r^2}$$

where, τ_f is the shear force at failure, r is the radius of the composite specimen, and L_f is the load at failure.

Acoustic emission method detects defects using sounds generated by the defects themselves. When a material is under stress, acoustic waves are generated by the transient release of strain energy caused by sudden internal displacements and spatial crack surface oscillations. Sensitive acoustic transducers are used to detect the waves. The various attributes of acoustic emission are counts, risetime, amplitude, threshold, and duration. These attributes can be employed alone or in combination to detect, localize, assess, or monitor failure.

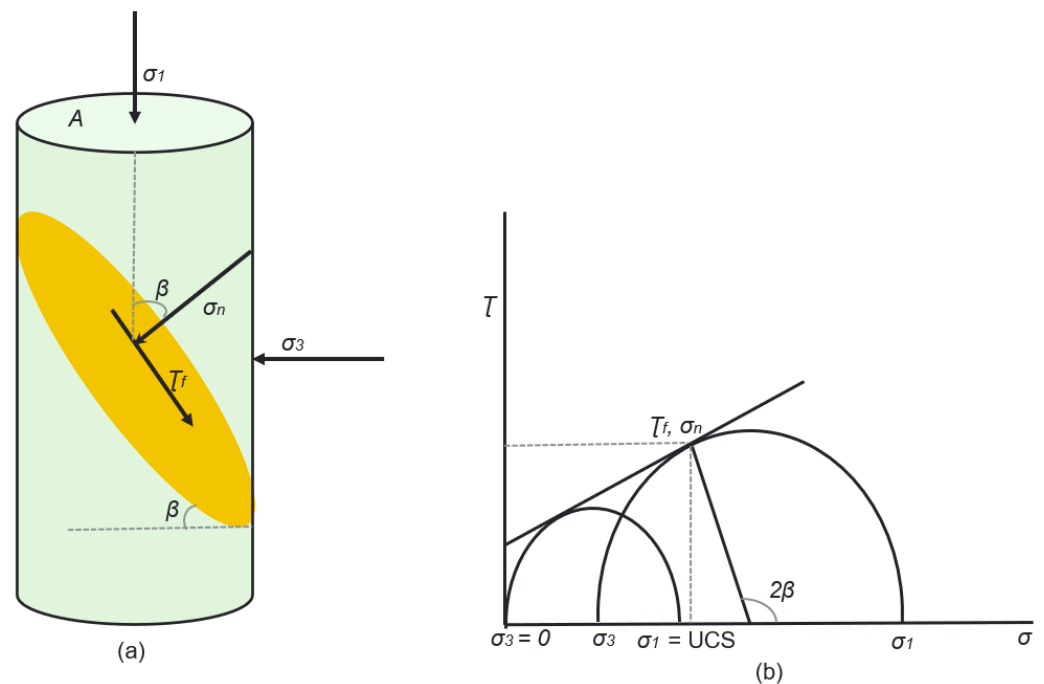


Figure 3. Stresses at failure. (a) Illustration of a cylindrical sample (top circle area A) with a bedding plane at an angle β under a confining pressure σ_3 and maximum compressive stress or axial stress σ_1 . (b) The normal stress σ_n and shear stress T_f on the plane correspond to the point where the Mohr circle hits the linearized Mohr failure envelope [20] (p. 88).

Only acoustic emission counts are acquired using one sensor mounted at the top of our specimen. It was discovered that there is a significant common trend in the variation in acoustic emission activity as a function of strain in each specimen. As a result, each specimen's failure is governed by similar fracture processes. Comparison of the acoustic emission count and variations in P- or S-wave velocities during deformation provides considerable insight into the mechanical processes at work [23].

A rock specimen's deformation history may be categorized into five distinct categories:

1. The specimen's initial compaction is caused by the preferential closure of cracks normal to the principal compression axis. This region is associated with low acoustic emission activity and an increase in P- and S-wave velocities.
2. A quasi-linear elastic region with constant elastic wave velocity.
3. Micro-crack initiation and extension, with an increasing acoustic emission count, when cracks develop predominantly parallel to the principal compression axis.
4. Macro-cracks form through coalescence of micro-cracks as the acoustic emission count saturates and the P- and S-wave velocities decrease sharply.
5. Shear faults are formed when macro-cracks combine. On the shear fault, frictional sliding occurs.

In most cases, it is difficult to distinguish all five regions since some are short-lived or absent in relation to nearby regions, or occur simultaneously, resulting in a combined region effect. The usage of velocity and acoustic emission activities as a function of strain was split into four stages in mortar [24]: crack closure (1), linear elastic (2), stable crack growth (3), and unstable crack growth stage (4). The third region of a rock specimen corresponds to the stable crack growth stage in mortar, whereas the fourth and fifth region correspond to the unstable crack growth stage.

A schematic diagram of distinct events/regions during the deformation of a rock/concrete specimen is shown in Figure 4. The green vertical arrows represent the direction of axial stress, which represents the principal compression axis. Region 2 is not depicted here since it lacks a visually distinct feature. Region 1 corresponds to a compaction event, whereas

regions 3 and 4 correspond to a multi-cracking event, and region 5 corresponds to a sliding event. The green slanting arrows in region 5 represent the sliding motion.

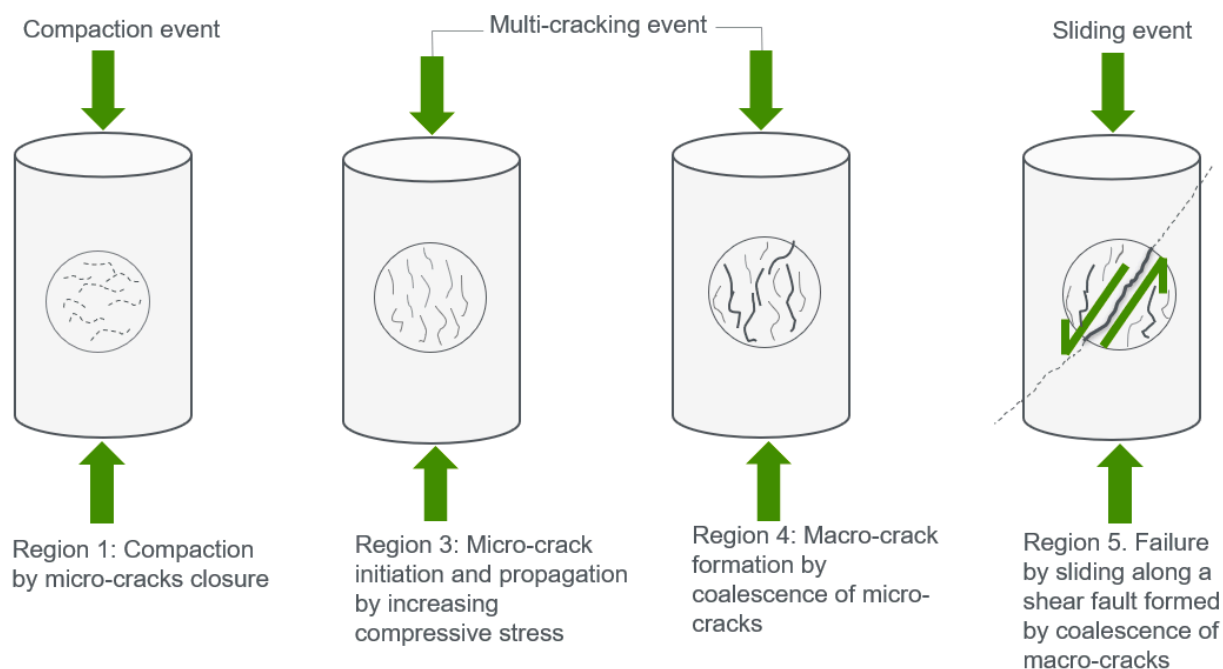


Figure 4. Schematic diagram of distinct events/regions during deformation of a rock/concrete specimen.

3. Results

The compressive strength of cement, formation, and composite cement–formation specimens, as well as the shear bond strength of the composite are shown in Table 3. Unconfined compressive strength (UCS) is the most widely used rock property. It is worth mentioning that Berea’s UCS of 32.8 MPa [22] is lower than the CS of 58 MPa at P_c of 10 MPa (Table 3). Similarly, UCS of 50 MPa utilizing UCA [15] is lower than CS of 65.6 MPa at P_c of 10 MPa with improved cement (Table 3).

Table 3. The mean compressive and shear bond strength of cement, formation, and composite cement–formation specimens at a confining pressure of 10 MPa.

Specimen	No. of Samples	Compressive Strength (MPa)	Shear Strength (MPa)
Berea	3	58 ± 2.65	-
Torrey	2	62	-
Cement	5	50 ± 3.24	-
Improved cement	2	65.6 ± 3.67	-
Cement–Berea	3	73.43 ± 3.83	31.8 ± 1.66
Cement–Torrey	3	54.3 ± 2.84	23.53 ± 1.23
Improved cement–Berea	4	71.35 ± 8.15	30.89 ± 3.53

Shear bond strength for cement–Castlegate sandstone of 4.5 Mpa [12] by push-out tests and 1.7 MPa [4] for cement–Berea sandstone were reported. Please note that [4] used Class H cement and their composite sample was made with cement and formation cores in a series arrangement. Shear bond strengths of 2.76–6.9 MPa were found between cement and shale [14]. Lower values in this study are due to the following factors: (a) unconfined conditions result in lower strengths [20] (p. 104); (b) multiple forces act at the interface,

rendering shear bond studies in most tests inconclusive [14]; and (c) cement–shale shear bond strength is lower than cement–sandstone shear bond strength [4].

Initial compaction of the specimen is characterized by a short-lived acoustic emission activity and an increase in velocity. The multi-cracking stage is characterized by the formation and propagation of both micro-cracks and macro-cracks. As a result of the complex multi-scale structure, micro-cracking initiates and accumulates, forming a fracture zone surrounding the starting point of the eventual macro-crack [25]. During the macro-crack formation and propagation, the acoustic emission counts exceed the sensor's limit, leading to the acoustic emission peaks. The acoustic emission peaks may be sensor-dependent and/or arbitrarily set. As a result, it is critical to maintain the sensor and its setting throughout the experiment. As confirmed by the velocity decrease and acoustic emission counts, numerous cracking incidents have a detrimental effect on the material durability or damage tolerance. The cracking process then repeats itself, with the formation of a new micro-scale crack leading to a new macro-scale crack. With increasing stress, newly developed macro-cracks show larger strain amplitudes. The acoustic emission count remains constant in the post-cracking stage because matrix cracks are saturated and the accumulated damage hinders acoustic emission wave propagation.

3.1. Whole Specimen Analysis

Compaction, multi-cracking, and sliding are three distinct and dominant events in the Berea sandstone specimen (Figure 5a). Region 1 corresponds to a compaction event, whereas regions 3 and 4 correspond to a multi-cracking event, and region 5 corresponds to a sliding event. Similar to Berea, the Torrey sandstone specimen (Figure 5b) exhibits three dominant events: compaction, multi-cracking, and sliding. The acoustic emission peaks in event 1 show that Torrey has a larger number of macro-cracks of smaller strain amplitudes generated from pre-existing micro-cracks than Berea. The acoustic emission peaks in event 2 show that Torrey also has a higher number of macro-cracks generated from newly formed micro-cracks than Berea. The total number of acoustic emission peaks in Figure 5 for Berea is 5 and Torrey is 26. Higher porosity and permeability in Berea (Table 1) may result in more empty space for particles to slide and interconnect more efficiently than in Torrey. As a result, the stress distribution in Berea is better. Torrey has more disconnected/isolated macro-cracks before a few of them merge to form a failure plane for sliding. Please note that the compressive strength values of Torrey (62 MPa) and Berea (58 MPa) are quite similar (Table 3), therefore the strength values alone would not provide this insight into their internal structure.

The pure cement specimen (Figure 5c) contains fewer pre-existing micro-cracks than the sandstone specimen, resulting in short-lived compaction event 1. Macro-cracks generated from pre-existing micro-cracks (acoustic emission peaks in event 1) do not demonstrate a strain amplitude increase with stress. Macro-cracks generated from new micro-cracks increase in strain amplitude with stress, as shown in event 2 of the pure cement specimen. The total number of acoustic emission peaks in Figure 5c for pure cement is 12, which is more macro-cracks than Berea (5) but less than Torrey (26).

Improved cement with compressive strength of 65.6 MPa is higher than 50 MPa for pure cement (Table 3). In improved cement, the initial compaction event 1 is absent as there is no increase in velocity observed (Figure 5d). This is because there are few (closed) or no pre-existing micro-cracks. The total number of acoustic emission peaks in Figure 5d for improved cement is 37. As the structure is denser in improved cement than pure cement [15], a larger number of isolated macro-cracks occur before a few of them join to create a failure plane for sliding.

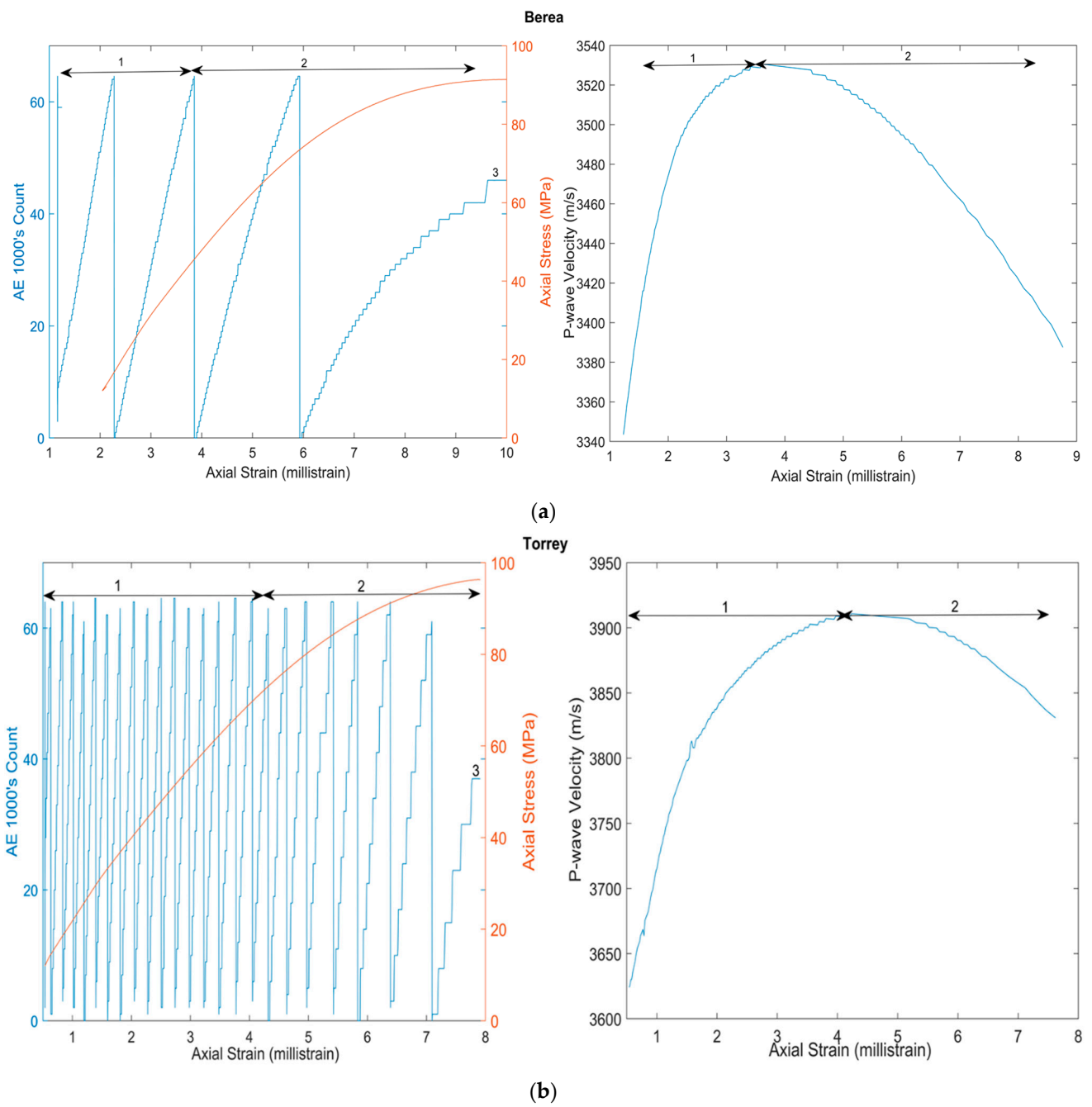


Figure 5. Cont.

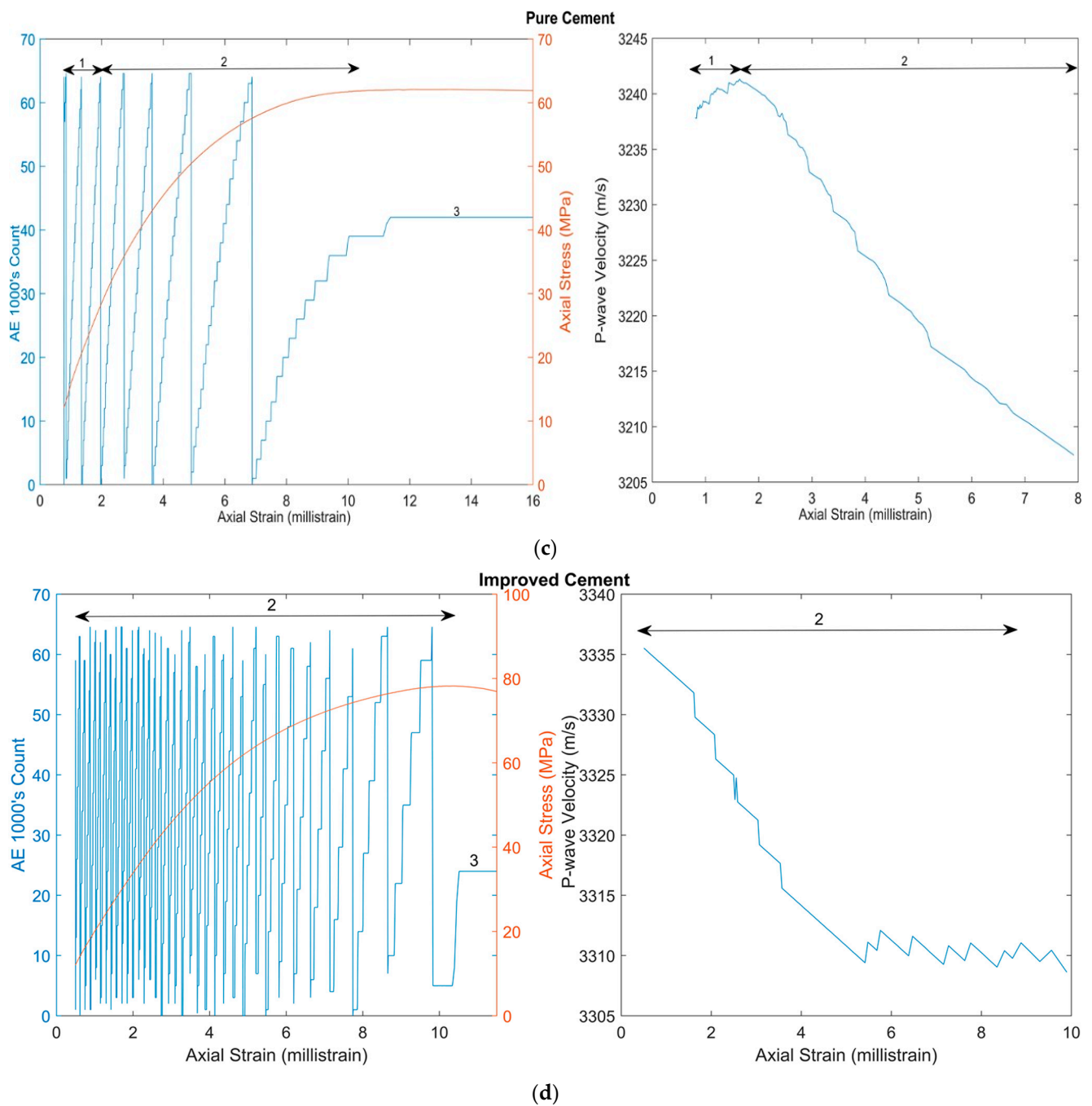


Figure 5. Failure analysis in a whole specimen. Acoustic emission (AE) counts in blue and axial stress in red are shown as a function of axial strain for (a) Berea (b) Torrey (c) pure cement and (d) improved cement in the left plots. The plots depict three distinct events: (1) compaction, (2) multi-cracking, and (3) sliding. The right plots show the P-wave velocities as a function of axial strain.

3.2. Composite Specimen Analysis

We found that the composite cement–sandstone specimen fails at the interface rather than in the cement because failure at the interface occurs at a lower stress level than that necessary to generate a new fault in the cement. Our composite specimens (Figure 6) reveal a combination of sandstone compaction (more pre-existing micro-cracks leading to macro-cracks from acoustic emission peaks in event 1) and cement multi-cracking (more macro-cracks from acoustic emission peaks in event 2) leading to shear failure. The cement–Berea (73.43 MPa) composite specimen has a higher compressive bond strength

than any of its constituents, Berea (58 MPa) or cement (50 MPa). Initial compaction of the cement–Torrey composite specimen (Figure 6b) is characterized by long-lived acoustic emission activity and an increase in velocity, as Torrey has a larger number of pre-existing micro-cracks. Table 3 shows that cement–Berea (31.8 MPa) bonding is stronger than cement–Torrey (23.53 MPa) bonding. This strength difference may be attributed to Berea’s higher porosity and permeability. Higher porosity might lead to better stress distribution and thus, attributing to the greater strength, as seen in the whole specimen case. Furthermore, higher permeability corresponds to a well-connected pore system, allowing more cement to fill the pore spaces, which leads to better bonding between the cement and formation [26].

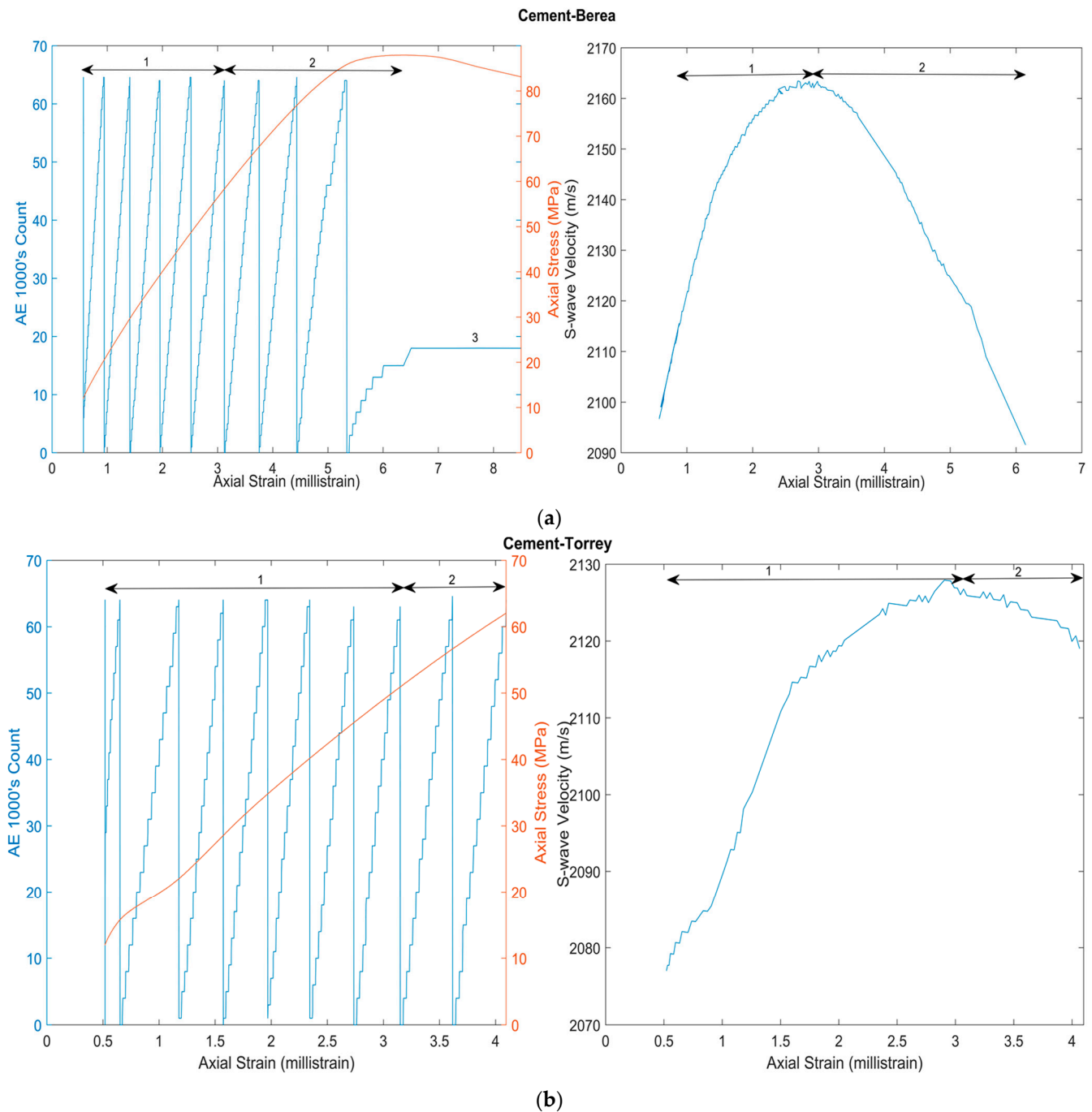


Figure 6. Cont.

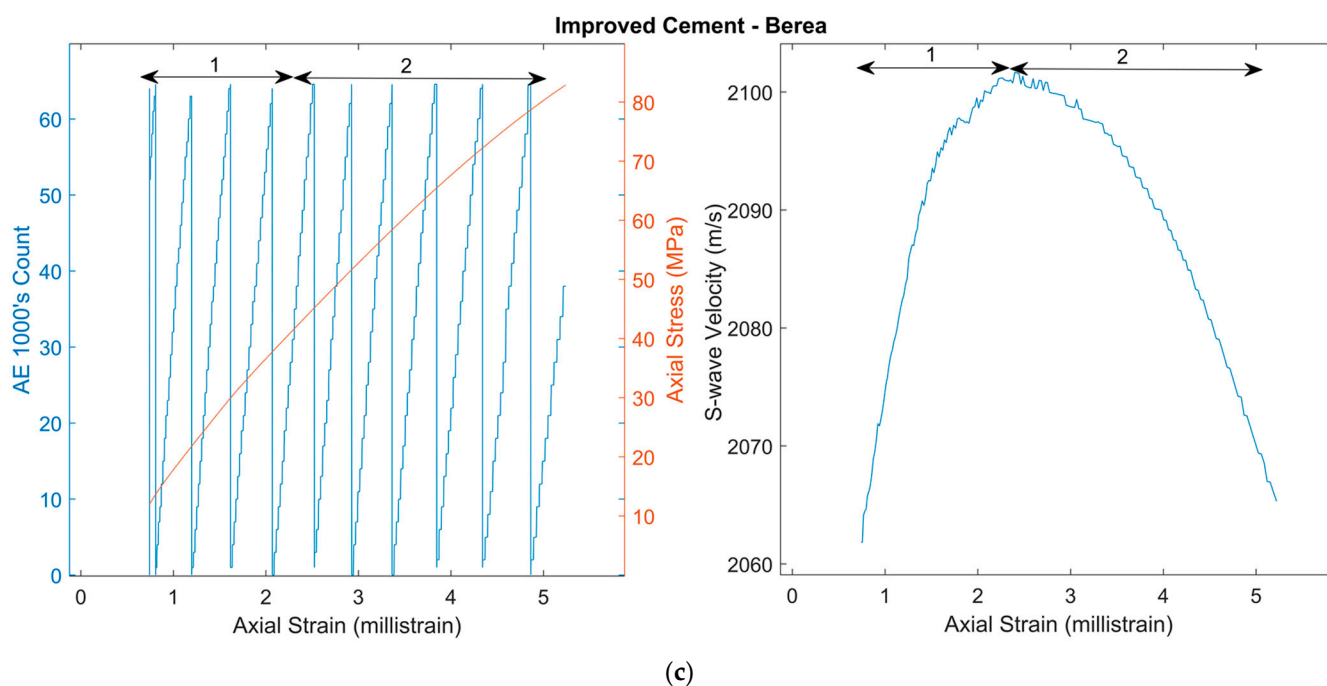


Figure 6. Failure analysis in a composite specimen. Acoustic emission (AE) counts in blue and axial stress in red are shown as a function of axial strain for (a) cement–Berea, (b) cement–Torrey, and (c) improved cement–Berea composite specimen in the left plots. The fracture mechanism is a combination of features observed in both cement and sandstone. The right plots show the S-wave velocities as a function of axial strain.

The shear bond strength of cement–Berea (31.8 MPa) and that of improved cement–Berea (30.89 MPa) are very close. The total number of acoustic emission peaks in Figure 6 for cement–Berea is 11 and that of improved cement–Berea is 12. Despite similar bond strengths and total number of macro-cracks, the composite specimen shows a slightly larger number of new isolated macro-cracks (acoustic emission peaks in event 2) in improved cement–Berea (7) than pure cement–Berea (5) in Figure 6. More isolated macro-cracks point to a lower damage tolerance in improved cement. Cement strength retrogression is an issue in some situations, such as deeper and thermal wells, where improved cement is still preferable [16].

Our method relates the material bonding to the number of macro-cracks generated by counting the acoustic emission peaks. When comparing materials, it is critical to use the same acoustic emission sensor and instrument setting to keep the acoustic emission counts that define the acoustic emission peaks consistent. This integrated approach is an excellent method to compare various specimens, however, the exact number of cracks generated may differ owing to the arbitrary definition of acoustic emission peaks. As a result, an imaging technique might be helpful in validating the findings for future research.

We attempted to keep our sample preparation protocol consistent, but unknown variables may still exist. One such factor is the variation due to change in curing and testing conditions. Future studies should identify and control more factors for enhanced accuracy.

4. Conclusions

Sample preparation procedures are essential for consistent results and accurate forecasts by reducing the number of variables. The fracture mechanism that causes the failure in cement formation and composite cement–formation specimens under downhole conditions is described using an acoustic emission count in conjunction with velocities and strain data. The ultimate failure in all specimens is caused by the development of fracture process zones from micro-cracks (acoustic emission count increase) progressing to macro-cracks (acoustic emission peaks), and the coalescence of macro-cracks leading to shear fault. Although the

three dominant events of compaction, multi-cracking, and sliding may be present, there are some differences related to the basic structure of each specimen.

Because the compressive strength values of Torrey (62 MPa) and Berea (58 MPa) are so close, the strength values alone would not reveal anything about their internal structure: Torrey has more pre-existing micro-cracks than Berea, and Berea has more empty space for particle movement to slide and interconnect more effectively than Torrey.

A compaction event is short-lived (pure cement) to absent (improved cement) due to the decreasing number of pre-existing micro-cracks. A larger number of isolated macro-cracks are formed in improved cement, indicating a denser structure. The denser structure is also confirmed by a higher compressive strength in improved cement (65.6 MPa) compared to pure cement (50 MPa).

Pure cement binds better with Berea (31.8 MPa) than Torrey (23.53 MPa) based on the shear bond strength values of the composite specimen. Although the shear bond strengths of Berea with pure cement (31.8 MPa) and improved cement (30.89 MPa) are very close, pure cement might pair better with Berea than improved cement due to higher damage tolerance, except where cement retrogression issues exist. Thus, our approach offers additional information for pairing the appropriate cement formulation to a formation rock by assessing its strength and damage tolerance.

Author Contributions: Conceptualization, A.P.B. and P.J.B.; methodology, A.P.B.; data analysis, A.P.B.; investigation, A.P.B.; writing—original draft preparation, A.P.B.; writing—review and editing, P.J.B.; project administration, A.P.B. All authors have read and agreed to the published version of the manuscript.

Funding: This research received no external funding.

Acknowledgments: The authors thank Roland Martinez for sample preparation and acoustic measurements.

Conflicts of Interest: The authors declare no conflict of interest.

References

1. Parcevaux, P.; Sault, P. Cement Shrinkage and Elasticity: A New Approach for a Good Zonal Isolation. In Proceedings of the SPE Annual Technical Conference and Exhibition, Houston, TX, USA, 16–19 September 1984. [\[CrossRef\]](#)
2. Carpenter, R.; Brady, J.; Blount, C.G. The Effects of Temperature and Cement Admixes on Bond Strength. *J. Pet. Technol.* **1992**, *44*, 936–941. [\[CrossRef\]](#)
3. Bois, A.-P.; Garnier, A.; Rodot, F.; Saint-Marc, J.; Aimard, N. How To Prevent Loss of Zonal Isolation Through a Comprehensive Analysis of Microannulus Formation. *SPE Drill. Complet.* **2011**, *26*, 13–31. [\[CrossRef\]](#)
4. Radonjic, M.; Oyibo, A. Experimental evaluation of wellbore cement-formation shear bond strength in presence of drilling fluid contamination. In Proceedings of the 5th International Conference on Porous Media and Their Applications in Science, Engineering and Industry, Kona, HI, USA, 22–27 June 2014.
5. De Andrade, J.; Sangesland, S.; Skorpa, R.; Todorovic, J.; Vrålstad, T. Experimental Laboratory Setup for Visualization and Quantification of Cement-Sheath Integrity. *SPE Drill. Complet.* **2016**, *31*, 317–326. [\[CrossRef\]](#)
6. Evans, G.W.; Carter, L.G. Bonding Studies of Cementing Compositions to Pipe and Formations. In *Drilling and Production Practice*; American Petroleum Institute: New York, NY, USA, 1962.
7. Peterson, B. Bond of cement compositions for cementing wells. In Proceedings of the 6th World Petroleum Congress, Frankfurt am Main, Germany, 19–26 June 1963.
8. Carter, L.; Evans, G. A Study of Cement-Pipe Bonding. *J. Pet. Technol.* **1964**, *16*, 157–160. [\[CrossRef\]](#)
9. Zhang, Z.; Scherer, G.W.; Prud'Homme, R.K. Adhesion and Bonding Between Steel Pipe and Cement/Spacer/Mud System. In Proceedings of the 9th International Conference on Fracture Mechanics of Concrete and Concrete Structures, Berkeley, CA, USA, 29 May–1 June 2016; pp. 22–25. [\[CrossRef\]](#)
10. Lamik, A.; Pittino, G.; Prohaska-Marchried, M.; Krishna, R.; Thonhauser, G.; Antretter, T. Evaluation of Cement-Casing & Cement-Rock Bond Integrity During Well Operations. In Proceedings of the SPE/IADC Middle East Drilling Technology Conference and Exhibition, Abu Dhabi, United Arab Emirates, 25–27 May 2021. [\[CrossRef\]](#)
11. API. *Recommended Practice for Testing Well Cements*; American Petroleum Institute: New York, NY, USA, 2005; pp. 1–146.
12. Opedal, N.; Todorovic, J.; Torsaeter, M.; Vrålstad, T.; Mushtaq, W. Experimental Study on the Cement-Formation Bonding. In Proceedings of the SPE International Symposium and Exhibition on Formation Damage Control, Lafayette, LA, USA, 26–28 February 2014. [\[CrossRef\]](#)

13. Ladva, H.K.J.; Craster, B.; Jones, T.G.J.; Goldsmith, G.; Scott, D. The Cement-to-Formation Interface in Zonal Isolation. In Proceedings of the IADC/SPE Asia Pacific Drilling Technology Conference and Exhibition, Kuala Lumpur, Malaysia, 13–15 September 2004. [[CrossRef](#)]
14. Liu, X.; Nair, S.D.; Cowan, M.; van Oort, E. A Novel Method to Evaluate Cement-Shale Bond Strength. In Proceedings of the SPE International Symposium on Oilfield Chemistry, The Woodlands, TX, USA, 13–15 April 2015. [[CrossRef](#)]
15. Bathija, A.P.; Martinez, R. An integrated approach to understand the failure mechanism in cement and formation. In *SEG Technical Program Expanded Abstracts*; Society of Exploration Geophysicists: Houston, TX, USA, 2020; pp. 2535–2539.
16. Murtaza, M.; Rahman, M.K.; Al-Majed, A.A.; Samad, A. Mechanical, Rheological and Microstructural Properties of Saudi Type G Cement Slurry with Silica Flour Used in Saudi Oil Field under HTHP Conditions. In Proceedings of the SPE Saudi Arabia Section Technical Symposium and Exhibition, Al-Khobar, Saudi Arabia, 19–22 May 2013. [[CrossRef](#)]
17. Reddy, B.R.; Zhang, J.; Ellis, M. Cement Strength Retrogression Issues in Offshore Deep Water Applications—Do We Know Enough for Safe Cementing? In Proceedings of the Offshore Technology Conference, Houston, TX, USA, 2–5 May 2016. [[CrossRef](#)]
18. Donath, F.A. Experimental Study of Shear Failure in Anisotropic Rocks. *GSA Bull.* **1961**, *72*, 985–989. [[CrossRef](#)]
19. Jaeger, J.C.; Cook, N.G.; Zimmerman, R. *Fundamentals of Rock Mechanics*; John Wiley & Sons: Hoboken, NJ, USA, 2009.
20. Zoback, M.D. *Reservoir Geomechanics*; Cambridge University Press: Cambridge, UK, 2010.
21. Vernik, L.; Lockner, D.; Zoback, M.D. Anisotropic strength of some typical metamorphic rocks from the KTB pilot hole, Germany. *Sci. Drill.* **1992**, *3*, 153–160.
22. Bathija, A.P.; Batzle, M.L.; Prasad, M. An experimental study of the dilation factor. *Geophysics* **2009**, *74*, E181–E191. [[CrossRef](#)]
23. Sammonds, P.; Ayling, M.; Meredith, P.; Murrell, S.; Jones, C. A laboratory investigation of acoustic emission and elastic wave velocity changes during rock failure under triaxial stresses. In Proceedings of the ISRM International Symposium, Pau, France, 30 August–2 September 1989.
24. Elaqla, H.; Godin, N.; Peix, G.; R’Mili, M.; Fantozzi, G. Damage evolution analysis in mortar, during compressive loading using acoustic emission and X-ray tomography: Effects of the sand/cement ratio. *Cem. Concr. Res.* **2007**, *37*, 703–713. [[CrossRef](#)]
25. Tsangouri, E.; Michels, L.; el Kadi, M.; Tysmans, T.; Aggelis, D.G. A fundamental investigation of textile reinforced cementitious composites tensile response by Acoustic Emission. *Cem. Concr. Res.* **2019**, *123*, 105776. [[CrossRef](#)]
26. Bathija, A.P.; Sengupta, M.; Eichmann, S.L. Cement to formation bond strength evaluation using image analysis. In Proceedings of the First International Meeting for Applied Geoscience & Energy, Denver, CO, USA, 26 September–1 October 2021.